# Starshade Technology Development Activity Milestone 7A: Demonstration of Dimensional Stability of Perimeter Truss Bay Longeron and Node

Manan Arya, David Webb, Flora Mechentel, S. Case Bradford, Doug Lisman,
*Jet Propulsion Laboratory, California Institute of Technology, Pasadena CA*

Eric Kelso, Andrei Iskra, Gregg Freebury,
*Tendeg, Louisville CO*

Jeremy Senne, Charles Tan, and Aaron Armour
*Applied Composites, San Diego CA*

July 10, 2020

**Revision History**

| Revision | Authors | Description |
|---|---|---|
| 10 July 2020 | - | Initial release |

# Contents

# Executive Summary

We present experimental results that meet the requirements of Milestone 7A of the Starshade Technology Activity S5. Full-scale medium-fidelity test articles of critical components of the perimeter truss – the longeron and the node – were constructed. These test articles were thermal cycled at least 50 times (between 70 °C and −25 °C), and their critical dimensions were measured at regular intervals using a MicroVu measurement system, which consists of a digital microscope on a two-axis translation stage. Applied Composites fabricated the test articles based on JPL designs, and testing was performed by Tendeg at their facility in Louisville, Colorado. The change in critical dimensions of the longerons and the nodes were measured to be less than 27 µm and 25 µm, respectively. Compared against the $3\sigma$ requirement for the dimensional changes of the longeron and the node – 56 µm for both – we report large margins of 108% and 125%, respectively.

# 1 Introduction

This report addresses the experimental verification of the S5 Milestone 7A [1]:

> Truss Bay longeron and node subassemblies demonstrate dimensional stability with thermal cycles (deployed) consistent with a total pre-launch petal position accuracy within ±300 µm.

The ±300 µm tolerance is an envelope of error sources that meets Key Performance Parameter 7 (KPP7); KPP7 specifies a degradation in instrument contrast of no more than $1.00 \times 10^{-12}$. Through the course of the work on this milestone, an updated envelope of ±340 µm was computed based on measured results that preserves the contrast allocation of $1.00 \times 10^{-12}$ to KPP7. As shown in Table 1, this contrast is sub-allocated to the three chief components of the petal position accuracy errors – radial bias, radial random, and tangential random. The instrument contrast is the mean value for a normal distribution with the specified $3\sigma$ standard deviation of the petal position error.

The error components are further sub-allocated to Milestone 7A (and the follow-on Milestone 7B), which is concerned with the dimensional stability of the truss bay, and Milestones 7C and 7D, which deal with the deployment accuracy of the Inner Disk Subsytem (IDS). Importantly, the sub-allocations to Milestones 7C and 7D were *not* changed during this update. The shape error allocations are written as $3\sigma$ values and sum in quadrature (root-sum-square) since they are considered to be independent and random.

| | **MS 7A, 7B** (µm) | **MS 7C, 7D** (µm) | **RSS total** (µm) | **Instrument Contrast** |
|---|---|---|---|---|
| Radial bias | 62 | 35 | 71 | $1.91 \times 10^{-13}$ |
| Radial random | 260 | 150 | 300 | $5.98 \times 10^{-13}$ |
| Tangential random | 80 | 120 | 144 | $2.10 \times 10^{-13}$ |
| Total | | | 340 | $1.00 \times 10^{-12}$ |

Table 1: Sub-allocation of KPP7 contrast levels to components of the petal position accuracy error. The original sub-allocations can be found in Appendix A.

For the purposes of Milestones 7A and 7B, which are concerned with the thermal-cycle stability of a single bay of the perimeter truss (a "bay" being the unit cell of the rotationally symmetric perimeter truss), these petal position accuracy errors can be allocated entirely to errors in the lengths of the bays.

For each bound on a petal position accuracy component, a corresponding bound on the truss bay length error can be calculated: meeting this truss bay length error bound guarantees that the bound on the petal position accuracy component is met. The relationship between bay length errors and the petal position accuracy components is calculated in Appendix B. The effect of coordinated modes of petal position error (e.g. ellipticity) is discussed in Appendix H.

The allocation of petal position accuracy error components to Milestones 7A and 7B is such that each component of petal position accuracy imposes an equivalent requirement on the bay length error, while ensuring that the instrument contrast allocation of $1.00 \times 10^{-12}$ is not exceeded. The requirements on bay length errors from each petal position accuracy component are listed in Table 2. As can be seen, if the bay

length error is less than 79.5 µm (at a $3\sigma$ level), then all components of the petal position accuracy error are within the allocation towards Milestone 7A.

| | **Petal position error** (µm) | **Bay length error** (µm) |
|---|---|---|
| Radial bias | 62 | 79.5 |
| Radial random | 260 | 79.5 |
| Tangential random | 80 | 79.5 |

Table 2: The chief components of the petal position errors can be translated to equivalent perimeter truss bay length errors. All errors are written as $3\sigma$ values.

For Milestone 7A, the bay length error is sub-allocated to the longeron and the node. The longeron and node length errors are expected to be random and uncorrelated, and, as such, add in quadrature. An equal sub-allocation of the bay length error of 79.5 µm leads to longeron and node length error allocations of 56.2 µm each.

The verification approach is to subject representative longeron and node test articles to 50 thermal cycles (70 °C to −25 °C), to measure critical dimensions at regular intervals, and verify that changes in critical dimension of each test article are less than 68.0 µm.

50 thermal cycles is a conservative upper bound for the number of on-ground thermal cycles and the expected 40 in-space thermal cycles for the reference Starshade Rendezvous Mission (SRM). This is based on the number of starshade retargeting maneuvers, each of which resets the orientation of the starshade with respect to the sun, thus causing thermal cycles. The expected extreme sun angles over the course of the mission are sun angle = 83° and sun angle = 0°. Over this range of sun angles, the expected temperature range for the longeron is 69 °C to −18 °C, and for the node is 59 °C to 9 °C. The experimental temperature range of 70 °C to −25 °C encompasses these values. Appendix G describes in further detail the thermal cycles that a starshade is expected to undergo during flight.

The objective of Milestone 7A is to verify that the longeron and node are dimensionally stable over the number of thermal cycles and the temperature range to which they will be subject. In establishing this reference, the longerons and nodes are not loaded during thermal cycling. Milestone 7B will then verify the stability of these components through thermal cycling when loaded, both in the deployed and stowed configurations. As an early assessment, post-Milestone 7A activities will include loaded testing of the existing hardware. Even though KPP7 covers pre-launch effects, the effects of both on-ground and in-space thermal cycling are housed under KPP7 currently.

There is an allocation separate from KPP7 to account for shape error from *uncertainty* in strain due to moisture loss in-space; this is expected to be a small effect and not drive performance. (A flight starshade will be designed to account for such strain, and the corresponding shape error is due to *uncertainty* in this strain, which is expected to be small.) However, strain due to moisture absorption (i.e. hygroscopic strain) is a source of noise for the work presented in this report, and its effect is discussed. Furthermore, coupon-level material testing to characterize hygroscopic strain effects is planned following Milestone 7A, and to decide whether work on *uncertainty* in hygroscopic strain should be planned for Milestone 7B.

This report is organized as follows: Section 2 describes the flight design of the starshade and its components, Section 3 describes the design and construction of the longeron and node test articles, and how they deviate from the flight design. Section 4 describes the test apparatus, Section 5 lists the test procedures, and Section 6 shows the data analysis methods and test results. Section 7 discusses the test results, and, finally, Section 8 provides conclusions.

# 2 Flight Design[1]

The S5 Technology Development Plan [1] uses the Starshade Rendezvous Mission (SRM) concept as its reference design. As shown in Figure 1, the SRM design is 26 m in diameter, with 24 8 m-long petals, and a 10 m-diameter inner disk [4]. The SRM concept is to launch a starshade to rendezvous with the WFIRST

[1]This section reproduces material from the S5 Milestone 7C Final Report [2] and the S5 Milestone 8A Final Report [3]

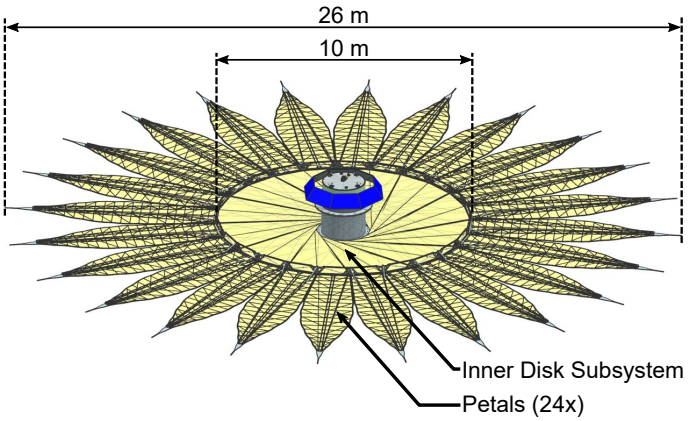


Figure 1: The Starshade Rendezvous Mission (SRM) design.

space telescope at the Sun-Earth L2. The starshade for the Habitable Exoplanet Observatory (HabEx) concept [5] uses the same architecture as the SRM starshade, but is double in size – 52 m in diameter with 24 16 m-long petals and a 20 m-diameter IDS. The work presented here is full-scale for the SRM concept, and half-scale for the HabEx starshade.

The mechanical architecture of the "wrapped" starshade design has been described before [6, 7, 8, 9]; here it will be summarized in brief. The starshade consists of a number of petals attached to the Inner Disk Subsystem (IDS). The IDS stows to a barrel-like shape around which the petals are wrapped. Deployment consists of two steps: first, the petals unfurl, and second, the IDS unfolds. During the first step of petal unfurling, the IDS remains latched in position and does not actuate. During the second step of IDS unfolding, the petals are fully deployed and have structural stiffness independent of the IDS. The petals and the IDS are exercised in sequence with a clean interface between them, and thus these two deployable subsystems can be studied independently.

As shown in Figure 1, the hub sits at the center of the IDS. To the hub are attached a number of spokes that connect the hub to the perimeter truss, which is on the outer circumference of the IDS. When fully deployed, the perimeter truss pulls the spokes into tension; the perimeter truss and the hub then go into compression. As such, the deployed IDS is a stiff preloaded structure, very much like a bicycle wheel. The final component of the IDS is a multilayer optical shield (OS) that rests below all the spokes. The OS makes the IDS opaque and is connected to both the hub and the perimeter truss.

## 2.1 Perimeter Truss

The perimeter truss is a stiff structure that reacts the tensile preload of the spokes in the deployed configuration. It provides attachment interfaces for each of the petals. The starshade perimeter truss draws heritage from the Astromesh antenna reflectors [10] that have been successfully deployed in space several times.

The perimeter truss is rotationally symmetric, consisting of 24 bays. Figure 2 shows a single truss bay. Each bay is a four-bar linkage; four rigid members – a longeron, a shorteron[2], and two nodes – are arranged in a planar parallelogram, linked to each other through revolute joints. (A revolute joint is a single-degree-of-freedom joint that allows for free rotation about a fixed axis, e.g. a scissor joint.) In this case, the revolute joints are realized using metallic pins affixed to the nodes that go through aligned bushing bore holes in the longerons and shorterons. By exercising the shear mechanism of each of the 24 four-bar linkages, the perimeter truss can transition from its deployed ring-like geometry to a stowed barrel-like form. The truss bay components critical to deployed shape stability are the longeron, the shorteron, and the two nodes. Since the shorterons and longerons are nearly identical in construction, the present milestone is concerned with the stability of only the longerons and the nodes. The critical dimensions of the longeron and the node are shown in Figure 2.

[2]The term "longeron" is commonly used in structural engineering for a load-bearing member in a framework. The term "shorteron" is specific to this starshade design: a shorteron is similar to a longeron, except shorter; hence "shorteron".

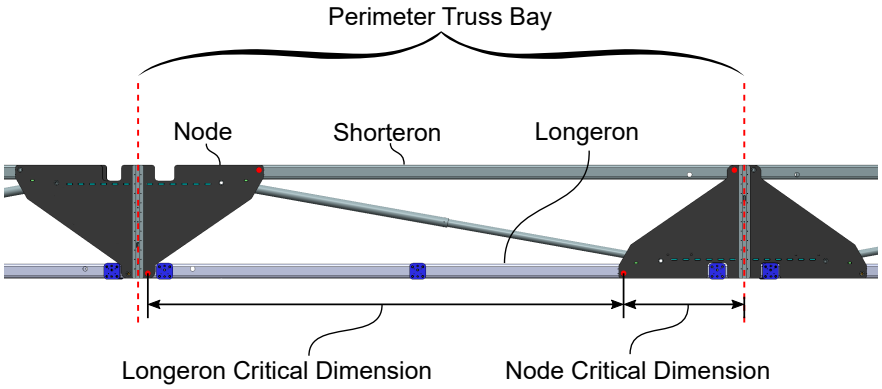


Figure 2: A single perimeter truss bay, showing key components and the critical dimensions of those components.

# 3 Test Articles

Three longeron test articles and three node test articles were manufactured by Applied Composites[3] in San Diego, California. Manufacturing was completed in March 2019. Of these, longerons 1 and 2 were used for the present work; longeron 3 was used exclusively for coefficient of thermal expansion (CTE) measurements for Milestone 8A prior to the present work, and these measurements required the disassembly of longeron 3 [3]. Additionally, longeron 2 was used for additional CTE measurements *during* the present work (due to schedule considerations), and was therefore subject only to 25 thermal cycles (as compared to the desired 50 thermal cycles). Longeron 1, however, was subject to the desired number of thermal cycles. Similarly, only nodes 2 and 3 were used for the present work; node 1 was not used since it was used exclusively for CTE measurement for Milestone 8A, which was conducted prior to the present work and required the disassembly of node 1 [3].

The subsections below detail the design and construction of these test articles.

## 3.1 Longerons

Each longeron test article consists of a 1005.25 mm-long carbon-fiber-reinforced plastic (CFRP) tube to which are bonded four metallic fittings made from low-CTE Invar 36. Two of these fittings represent interfaces to nodes; the other two represent interfaces to the petal. Figure 3 shows the design of the longeron test articles, as well as the critical node-interface-to-node-interface dimension that was measured for this experiment. This critical dimension is the length between the centers of two circular holes $u$ and $v$ on either end of the longeron. These holes pass through the entire longeron, and in flight, pins attached to nodes would pass through these holes to create revolute joints.

The 979 mm critical dimension of the longeron matches the flight design. The baseline design of the flight longeron is a square tube, though the exact cross-section geometry remains an open trade; here, a circular cross-section was used to provide uniform bending stiffness along all transverse axes. This axisymmetric design was driven by test considerations for Milestone 8A, for which this hardware was also used [3].

In flight, the longeron would have three petal interfaces; however, one of those petal interfaces is outboard of the node interfaces, and is therefore not in the critical load path between the node interfaces. As such, this outboard petal interface was not represented in these test articles.

The material for the CFRP tubes is a laminate of unidirectional (UD) M55J carbon fibers in a Patz PMT F-6 cyanate ester matrix. The laminate consists of 24 layers laid up the following stack: $[0°/64°/-64°]_8$. The fiber volume fraction of the tubes was designed to be 57%.

To achieve tight tolerances on the outer diameter of the longeron tube, "Smart Caul" technology was used to manufacture the tubes. CFRP plies pre-impregnated with the matrix were laid up over a cylindrical mandrel made from shape memory polymer, and then placed within a metallic female mold. Ply-placement

[3]Previously San Diego Composites.

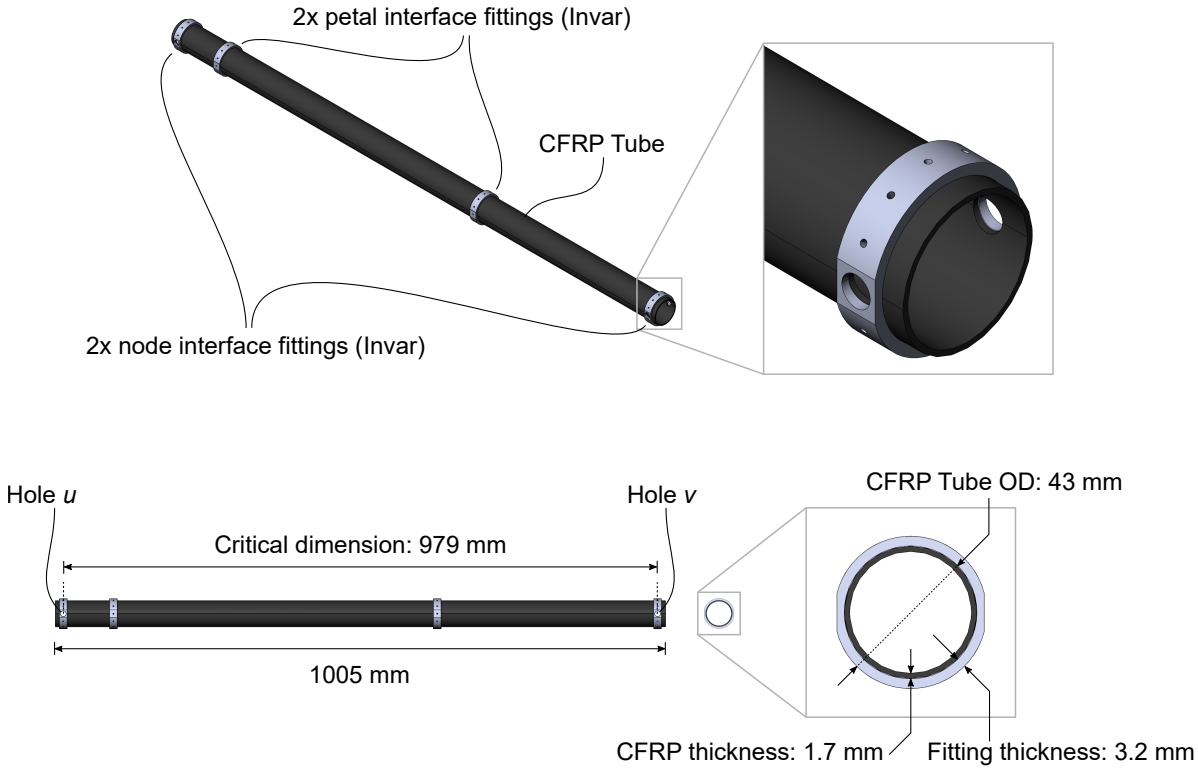


Figure 3: Design of the longeron test articles.

accuracy was measured (using "pi tapes") to be $\pm 0.5°$. The laminate was "reverse bagged", such that during curing pressure was applied from the interior of the tube outwards, conforming the laminate to the interior surface of the female mold.

After the CFRP tubes were cured, they were conditioned by thermal cycling them 5 times ($-40\,°C$ to $80\,°C$) to relieve internal stresses and to expel volatiles. Once conditioned, the four machined metallic fittings were injection bonded to the CFRP tubes using Loctite EA 9394, which is a two-part room-temperature-curing epoxy adhesive. Bond wire was used to obtain a uniform 127 µm-thick bondline. An assembly fixture was used during bonding to ensure consistent placement of the fittings. After bonding the metallic fittings, the test articles were conditioned again by thermal cycling them 10 times ($-40\,°C$ to $80\,°C$). Finally, holes $u$ and $v$ were match-drilled through the node interfaces.

These materials and manufacturing processes are considered to be reasonably flight-like.

## 3.2 Nodes

The node test articles exploit the symmetry in the flight design of the nodes, and represent only one-quarter of the flight node design. Figure 4 shows the design of the flight node and its relation to the quarter-node design that was fabricated. The flight node has two critical dimensions: widths on the wide and the narrow sides. The narrow side of the node is a shorter version of the wide side, and its behavior is expected to be similar to the wide side. The quarter-node test articles exploit this fact and represent only the wide side of the node. Additionally, because of its smaller size, the narrow side of the node has a smaller contribution to performance.

Figure 5 shows the design of the node test articles. The structure of each node test article is composed of four parts: two faceplates, one brace, and one fitting. The faceplates and brace are made from CFRP plates. The fitting is made of Invar 36. Additionally, two brass bushings are bonded to the faceplates where node has a revolute joint connection to the longeron. For Milestone 8A, which is concerned with the CTE of the nodes, the brass bushings were replaced with low-CTE Invar features for node 1 [3]. Node 1 was not used for the present work. Nodes 2 and 3, which were used here, retained the original brass bushings. It is

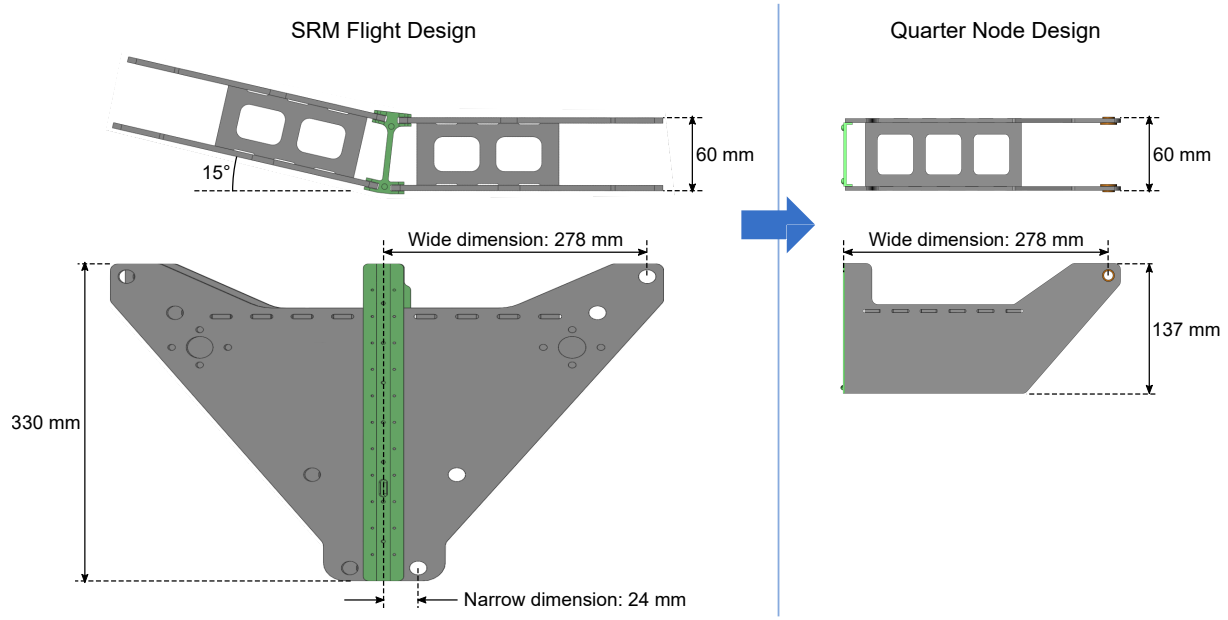


Figure 4: The node test article compared to the design of the flight node.

expected that the flight nodes would use Invar bushings; the use of brass bushings in nodes 2 and 3 is not expected to much affect the thermal-cycle-stability of the nodes.

As shown in Figure 5, the critical dimension of the node test article is the distance from the center of the circular hole $t$ on the faceplates to the end-edge $s$ of the test article (which represents the mid-plane of the flight node).

The CFRP plates used to make the faceplates and the braces consist of unidirectional M55J carbon fiber plies in a Patz PMT-F6 cyanate ester matrix. The laminate stack consists of 47 plies, and is symmetric: $[0°/45°/-45°/90°]_5[90°/45°/-45°/0°/-45°/45°/90°][90°/-45°/45°/0°]_5$. Cured plates were measured to be 3.12 mm thick, with a mean fiber volume fraction of 54.8%. Ply-placement accuracy was measured using a digital protractor to be $\pm 0.5°$. The faceplates and brace were cut out from these plates using a CNC (computer numerically controlled) waterjet cutter. After cutting, the faceplates and braces were conditioned through thermal cycling (5 cycles, $-40\,°C$ to $80\,°C$).

The assembly and bonding of each node test article was conducted on a fixture. The structural connection between each faceplate and the fitting is through a bonded lap joint, using room-temperature-curing epoxy EA 9394. Bond wire was used to obtain uniform 127 µm epoxy thickness. The brace was bonded to either faceplate on the through-thickness face. The bondline thickness was held to 127 µm using glass beads. The brass bushings were also bonded to the faceplates, around the cylindrical surface and also on the flange face. EA 9394 was used here, as well.

After bonding, the node test articles were conditioned using thermal cycling (10 cycles, $-40\,°C$ to $80\,°C$).

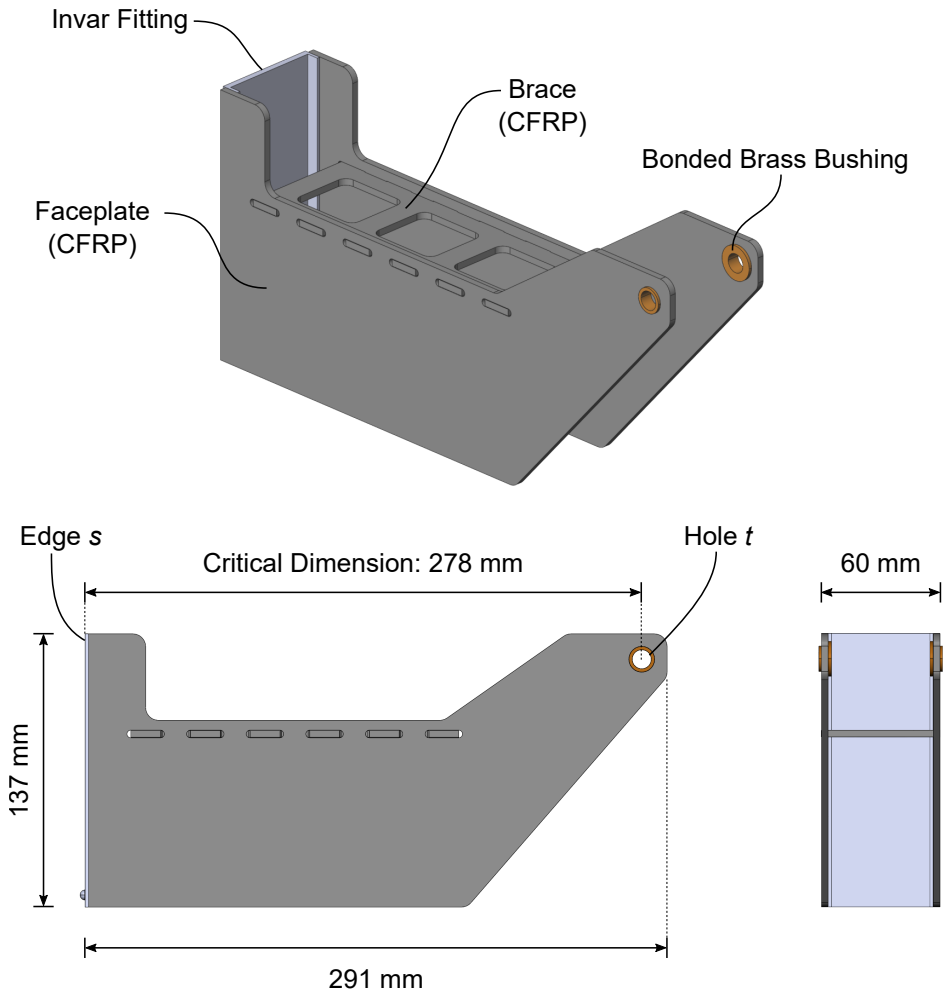


Figure 5: Design of the node test article.

# 4 Test Apparatus

## 4.1 Metrology

A MicroVu Excel 250ULC machine was used to measure the critical dimensions of the longerons and the nodes. This machine consists of a digital microscope mounted on an $(x, y)$-translation stage. Linear encoders on the two orthogonal axes of the translation stage are used to register microscope images in a global coordinate system. Test articles are placed on a transparent glass bed, which allows the microscope to use a combination of reflected and transmitted light for imaging. MicroVu software extracts the 2D location of edges of test articles from microscope images using a contrast-based edge-detection algorithm. The software can then output these 2D locations and key characteristics such as lengths between features.

The sources of measurement uncertainty in this system can be divided into two groups: uncertainty due to thermal strain of the linear encoders (the MicroVu machine does not measure its internal temperature and does not automatically compensate for this effect[4]), and repeatability errors (e.g. due to variations in the edge-detection algorithm, in microscope pointing from structural compliance of the machine, in plate-scale of the microscope, etc.). Of these, linear encoder thermal strain was identified to be the largest contributor, since this experiment was conducted over many months, with the MicroVu machine temperature varying over an estimated 3 °C range over this period. (This estimate is based on measurements of air temperature from an Omega weather logger placed next to the MicroVu machine over the latter portion of this experiment.)

Since the MicroVu internal temperature was not directly measured contemporaneously with test article measurements, it is not possible to correct the measurements for the thermal expansion of the linear encoders. Instead, conservative error bounds on the measured data are computed using the estimated temperature range of the MicroVu and the measured coefficients of thermal expansion (CTE) of the two linear encoders. The measurement of the encoder CTEs is described in Appendix D. The computation of the measurement uncertainty is described in Section 6.1.

## 4.2 Environmental Chambers

Two environmental chambers were used to conduct thermal cycling of the test articles: a Cincinnati Sub Zero (CSZ) ZPS-64-6-6-SC/WC chamber was used to thermal cycle the longerons and (for the final 30 thermal cycles) the nodes, as well. This chamber has a bed large enough to accommodate the longerons. For the first 20 thermal cycles for the nodes, a smaller environmental chamber – the SPX Thermal Product Solutions Tenney T10S-1.5 – was used. In both cases, thermocouples were used to monitor test article temperatures during the thermal cycles.

# 5 Test Procedures

Once manufactured, longerons 1 and 2, and nodes 2 and 3, were shipped from San Diego, California to Tendeg's facility in Louisville, Colorado. All thermal cycling relevant to the present milestone and metrology was conducted at Tendeg.

Prior to thermal cycling, the critical dimensions of test articles were measured using the MicroVu machine, to establish a baseline. Then, the test articles were thermal cycled in the environmental chambers. The temperature range during thermal cycles was 70 °C to −25 °C (except for the first 20 thermal cycles for the nodes, where the temperature range was was 70 °C to −20 °C). For the thermal cycles, a ramp rate of $2\,^{\circ}\mathrm{C\,min^{-1}}$ was used, with 1 hour holds the maximum and minimum temperature setpoints. Completing 10 thermal cycles with these parameters took approximately 36 hours. Table 9 and Table 10 in Appendix E list the dates, and the maximum and minimum temperatures recorded during the thermal cycling. During thermal cycling, the longerons were placed in an unstrained horizontal position, and the nodes were placed in an unstrained vertical position, as shown in Figure 6.

[4]Based on communications with MicroVu representatives. MicroVu software includes a non-default option to correct for encoder thermal strain using an operator-supplied MicroVu-internal temperature. However, this option was not discovered until partway through this work, and was not used moving forward to maintain consistency and continuity of measurements. Moreover, this option requires the operator to measure and supply a MicroVu-internal temperature; the capability to measure this temperature was not developed until after this work. MicroVu representatives have indicated that future MicroVu models currently under development will include internal thermometers to enable automatic compensation for encoder thermal strain.

(a) Longerons (b) Nodes

Figure 6: Test articles in the CSZ environmental chamber.

After a number of thermal cycles (either 5 or 10), the test articles were removed from the environmental chambers, placed on the MicroVu machine, and their critical dimensions were measured. Table 3 and Table 4 show the dates of these measurements in relation to the dates of the thermal cycles.

For each measurement, both sides of the test article were measured. Both the longeron and the node test articles have bilateral mirror symmetry, and the critical dimension lies in the center plane. Thus, measuring both sides and averaging produces a good estimate of the critical dimension. For each side of the test articles, at least three repeated measurements were taken in sequence; the results from these repeated measurements were averaged to reduce the effect of random errors.

The MicroVu was programmed to measure the critical dimensions of the test articles by taking a number of microscope images of relevant features, and using its contrast-based edge-detection algorithms, output the 2D locations of key geometry. For each side of the longerons, the MicroVu was programmed to detect the inner circular edges of the holes $u$ and $v$ (see Figure 3 for their locations). The longeron critical dimension was then calculated as the distance between the centers of circles fit to the edges of the holes $u$ and $v$. For each side of the node, the MicroVu was programmed to detect the edge $s$ and the inner circular edge of the hole $t$ (see Figure 5 for the locations of these features). The node critical dimension was then calculated as the distance between a straight-line-fit through the detected edge $s$ and the center of a circle fit to the edge of the hole $t$.

In addition to measurements after every 5 or 10 thermal cycles, at some points the test articles were measured again without any intervening thermal cycles. These measurements are also listed in Table 3 and Table 4. As shown in Table 3, on 2019.12.04, longeron 1 was measured upon its return to Tendeg after having been shipped out to Northrop Grumman Innovative Systems (NGIS) in San Diego for work related to Milestone 8A; this measurement was done to assess changes in critical dimension due to shipping or moisture absorption. Additionally, after 20 thermal cycles, as shown in Table 3, the longerons were measured not once, but three times between 2019.06.13 and 2019.07.01 without any intervening thermal cycles. These three separate measurements were conducted to try and resolve apparent changes in the critical dimensions of the longerons; this was prior to the understanding that the thermal strain of the MicroVu machine could cause large apparent changes in dimensions. These three separate measurements are processed similarly to the others in this analysis. As shown in Table 4, on 2019.10.28, the nodes were measured after having been shipped out to NGIS in San Diego and returned to Tendeg; again, this was to assess changes in critical dimension due to shipping or moisture absorption. Additionally, as shown in Table 4, on 2019.11.08, the nodes were measured after a thermal soak (72 hours at 40 °C), which was conducted to try and remove

| | |
|---|---|
| 2019.05.31 | Measurement (Baseline) |
| 2019.06.05 | 10 thermal cycles complete |
| 2019.06.06 | Measurement (Post 10 thermal cycles) |
| 2019.06.13 | 20 thermal cycles complete |
| 2019.06.13 | Measurement (Post 20 thermal cycles 1) |
| 2019.06.18 | Measurement (Post 20 thermal cycles 2) |
| 2019.07.01 | Measurement (Post 20 thermal cycles 3) |
| 2019.07.12 | 25 thermal cycles complete |
| 2019.07.16 | Measurement (Post 25 thermal cycles) |
| 2019.12.04 | Measurement (Post shipment from and return to Tendeg) |
| 2019.12.07 | 35 thermal cycles complete |
| 2019.12.07 | Measurement (Post 35 thermal cycles) |
| 2019.12.09 | 45 thermal cycles complete |
| 2019.12.09 | Measurement (Post 45 thermal cycles) |
| 2019.12.11 | 55 thermal cycles complete |
| 2019.12.11 | Measurement (Post 55 thermal cycles) |

Table 3: Longeron timeline.

| | |
|---|---|
| 2019.04.17 | Measurement (Baseline) |
| 2019.04.22 | 10 thermal cycles complete |
| 2019.04.22 | Measurement (Post 10 thermal cycles) |
| 2019.10.28 | Measurement (Post shipment from and return to Tendeg) |
| 2019.11.08 | Measurement (Post thermal soak) |
| 2019.11.11 | 20 thermal cycles complete |
| 2019.11.11 | Measurement (Post 20 thermal cycles) |
| 2019.12.05 | 30 thermal cycles complete |
| 2019.12.05 | Measurement (Post 30 thermal cycles) |
| 2019.12.07 | 40 thermal cycles complete |
| 2019.12.07 | Measurement (Post 40 thermal cycles) |
| 2019.12.09 | 50 thermal cycles complete |
| 2019.12.09 | Measurement (Post 50 thermal cycles) |

Table 4: Node timeline.

absorbed moisture from the nodes.

Figure 7 shows the longeron and node test articles on the MicroVu machine. For each measurement, each longeron was set down on two 48 mm-tall flat-top metal blocks that raised the longeron above the glass bed of the MicroVu. The metallic node interfaces on the longerons have flat faces around where the interface hole is drilled (see Figure 3); at one end of each longeron, these flat faces were rested on the flat-top of a block to constrain the rotation of the longerons about the longitudinal axis. The cylindrical face of the CFRP tube of the other end of longeron rested on the flat-top of the other block. For each measurement, the nodes were also set down on two of the 48 mm-tall flat-top metal blocks. Both the longerons and the nodes were oriented on the MicroVu bed such that their critical dimensions were aligned with the $x$-axis of the MicroVu.

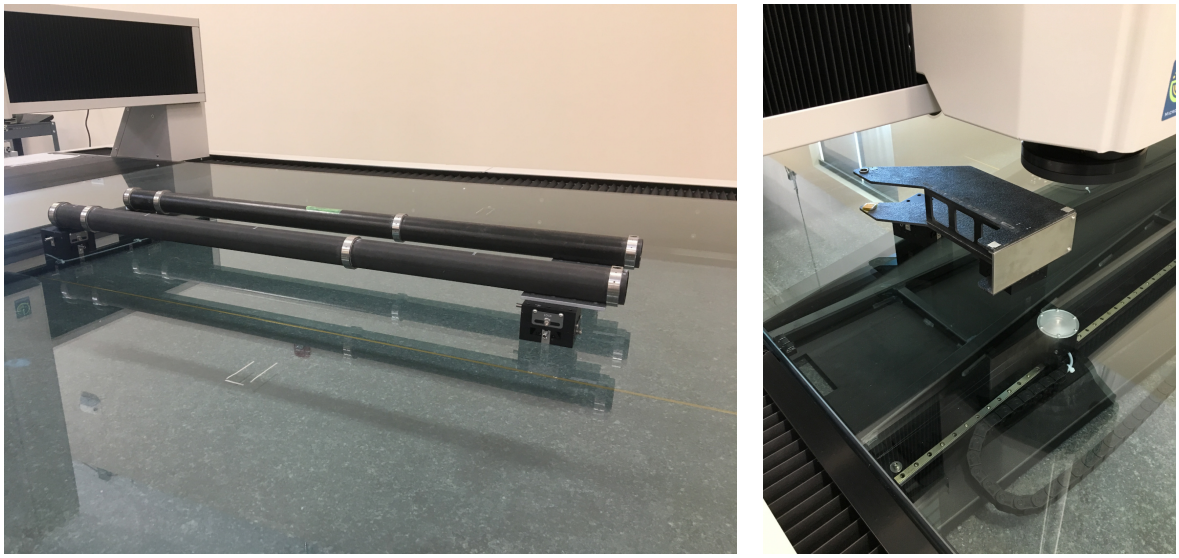

(a) (b)

Figure 7: Test articles on the MicroVu.

# 6 Test Results and Data Analysis

For each of the four test articles, the critical dimension is a scalar length. The data analysis for all test articles is identical, and thus will be described in generality, without reference to the specific test article. Denote the critical length as $L_i$, where $i$ is the number of thermal cycles after which the dimension is measured. Length $L_i$ is estimated as the mean of the lengths measured on the 'A' and the 'B' side of the test article, $A_i$ and $B_i$, respectively:

$$L_i = \frac{1}{2}\left(A_i + B_i\right) \tag{1}$$

The lengths on the 'A' and 'B' side are calculated as the mean of the measurements of these lengths over multiple trials; the number of these trials varied between 3 and 12:

$$A_i = \text{mean}\left(A_{i,1} + A_{i,2} + \dots\right) \tag{2}$$

$$B_i = \text{mean}\left(B_{i,1} + B_{i,2} + \dots\right) \tag{3}$$

where $A_{i,j}$ represents the length measured on the 'A' side after $i$ thermal cycles at the $j^{th}$ trial, and similarly for $B_{i,j}$.

The relevant metric for meeting the milestone is the change in the critical dimension from the baseline configuration, which is calculated as $\Delta L_i$:

$$\Delta L_i = L_i - L_0 \tag{4}$$

where $L_0$ is the dimension obtained at the baseline measurement.

Figure 8 and Figure 9 plot the changes in critical dimension $\Delta L_i$ for the two longerons and the two nodes, respectively. For completeness, Appendix F includes plots of the changes in the lengths on the 'A' and 'B' sides of the test articles.

## 6.1 Uncertainty Analysis

In a $\pm 1.1\,^{\circ}\text{C}$ range of its calibration temperature, the MicroVu Excel 250ULC has a stated length measurement accuracy of $\pm(5.5 + L/300)$µm where $L$ is the length being measured in millimeters [11]. However, the estimated temperature range of the MicroVu was $\pm 1.5\,^{\circ}\text{C}$ over this experiment, and thus the stated accuracy may not be applicable. To compute conservative measures of uncertainty for this experiment, the following approach is taken:

1. Estimate the measurement uncertainty based on the stated MicroVu accuracy of $\pm(5.5 + L/300)$µm
2. Estimate the measurement uncertainty based on a root-sum-square addition of error due to encoder thermal strain effects and error due to repeatability
3. For each test article, take the final measurement uncertainty to be the largest of the two values computed in Steps 1 and 2.

### 6.1.1 Measurement Uncertainty based on Stated MicroVu Accuracy

Using the stated MicroVu accuracy formula of $\pm(5.5 + L/300)$µm, with the relevant length $L = 979\,\text{mm}$ for the longeron, and $L = 278\,\text{mm}$ for the node, measurement errors of $\pm 8.8\,\mu\text{m}$ for the longeron and $\pm 6.4\,\mu\text{m}$ for the node are obtained.

### 6.1.2 Measurement Uncertainty from Encoder Thermal Strain and Repeatability

To estimate the uncertainty due to thermal strain of the MicroVu linear encoders, consider how this strain affects length measurements. The linear encoders act as length references for the MicroVu, and for a true part

length $L$, linear encoder CTE $\alpha$, and linear encoder strain $\epsilon_{encoder} = \alpha\Delta T$, the measured length $L_{measured}$ and the associated relative error is computed as follows:

$$L_{measured} = \frac{L}{1 + \epsilon_{encoder}} \tag{5}$$

$$\Rightarrow \frac{L - L_{measured}}{L} = \frac{\epsilon_{encoder}}{1 + \epsilon_{encoder}} \tag{6}$$

For both the longeron and the node, the critical dimensions were aligned with the $x$-axis, the corresponding linear encoder for which has CTE $\alpha = 4.9 \times 10^{-6}\,^{\circ}\mathrm{C}^{-1}$ (see Appendix D for a detailed description of the measurement of the encoder CTEs). Using $\Delta T = \pm 1.5\,^{\circ}\mathrm{C}$, the length measurement error $L - L_{measured}$ due to thermal strain of the machine can be computed: $\pm 7.2\,\mu\mathrm{m}$ for the longeron, and $\pm 2.1\,\mu\mathrm{m}$ for the node.

The measurement uncertainty due to repeatability errors is taken to be the length-invariant portion of the stated MicroVu accuracy; this amounts to $\pm 5.5\,\mu\mathrm{m}$ for both the longeron and the node. It is expected that the *length-dependent* portion of the stated MicroVu accuracy $(L/300)\mu\mathrm{m}$ is to account for machine thermal strain effects within a small temperature range. Using $\pm 5.5\,\mu\mathrm{m}$ as the uncertainty due to repeatability is also consistent with the observed repeatability of the measurement system[5].

Adding the thermal strain and repeatability contributions in quadrature, the following length measurement uncertainties are obtained: $\pm 9.1\,\mu\mathrm{m}$ for the longeron, and $\pm 5.9\,\mu\mathrm{m}$ for the node.

Now, comparing the values of measurement uncertainty obtained using the two different methods, and taking the largest for each test article, the following uncertainties are obtained: $\pm 9.1\,\mu\mathrm{m}$ for the longeron, and $\pm 6.4\,\mu\mathrm{m}$ for the node. These are taken to represent the uncertainty $u(X_i)$ in the length measurements $A_i$ and $B_i$ of the critical dimensions on side 'A' and 'B' of the test articles.

To go from an uncertainty $u(X_i)$ in the measurement of side lengths $A_i$ and $B_i$ to an uncertainty in the measurement of changes in critical dimension $u(\Delta L_i)$, standard rules of uncertainty propagation are used:

$$L_i = \frac{1}{2}(A_i + B_i) \tag{7}$$

$$\Rightarrow u(L_i) = \frac{1}{2}\sqrt{u(A_i)^2 + u(B_i)^2} \tag{8}$$

$$= \frac{1}{\sqrt{2}} u(X_i) \tag{9}$$

$$\Delta L_i = L_i - L_0 \tag{10}$$

$$\Rightarrow u(\Delta L_i) = \sqrt{u(L_i)^2 + u(L_0)^2} \tag{11}$$

$$= \sqrt{2}\, u(L_i) \tag{12}$$

$$= u(X_i) \tag{13}$$

It is found that the uncertainty in the *change in critical dimension* $\Delta L_i$ is equivalent to the uncertainty in the measurement of the length on either side of the part. Figure 8 and Figure 9 use these computed uncertainties for the four test articles as the error bars around the measured dimensional changes.

[5]Based on communications with MicroVu representatives, the length-invariant portion of the stated MicroVu accuracy $5.5\,\mu\mathrm{m}$ is indeed intended to capture repeatability errors at a $6\sigma$ level.

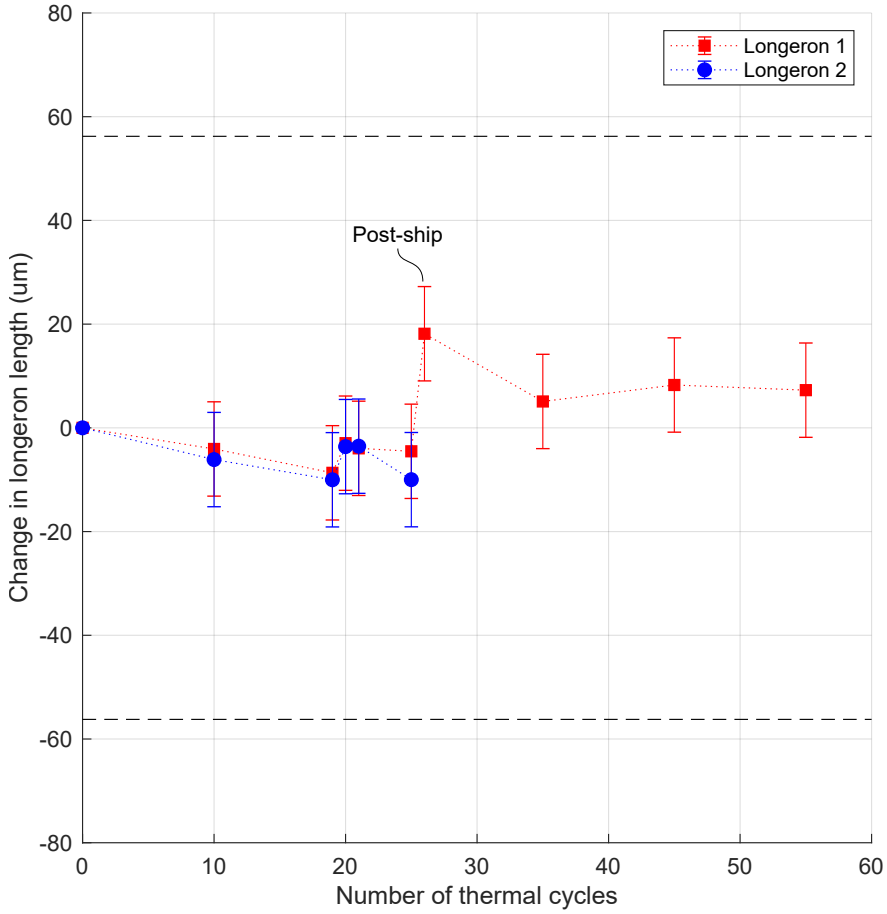


Figure 8: Change in the critical dimension of the longeron test articles over 55 thermal cycles. The dashed black lines represent the 56 µm allocation. Error bars capture measurement uncertainty. The clustered data at 20 thermal cycles represent 3 sequential measurements of the test articles without any intervening thermal cycles, i.e. these data were all taken with the test articles having been subject to 20 thermal cycles. After 25 thermal cycles, longeron 2 was used for supporting work on Milestone 8A which required the test article to be cut into sections; longeron 2 was not used for the present Milestone 7A beyond this point. The datum labeled "Post-Ship" was taken with the test article at 25 thermal cycles, after having been shipped from and back to Tendeg.

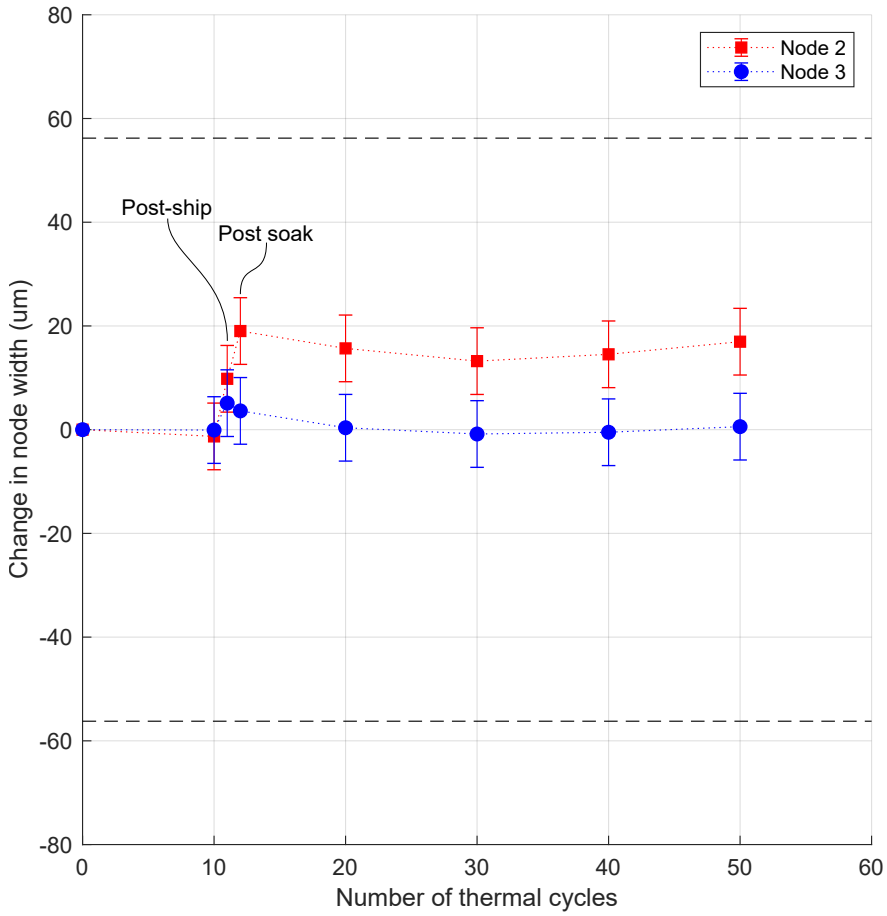


Figure 9: Change in the critical dimension of the node test articles over 50 thermal cycles. The dashed black lines represent the 56 µm allocation. Error bars capture measurement uncertainty. The data labeled "Post-Ship" were taken with the test article at 10 thermal cycles, after having been shipped from and back to Tendeg. The data labeled "Post-Soak" were taken after the test articles were subject a 72-hour soak at constant temperature, but still at 10 thermal cycles.

# 7 Discussion of Results

As can be seen from Figure 8 and Figure 9, the changes in critical dimensions of the nodes and the longerons over the 50 thermal cycles, accounting for measurement uncertainties, are well below the required $3\sigma$ allocation of 56 µm. The maximum change in dimensions for the longeron and the node consistent with the observations are 27 µm and 25 µm, respectively. As such, there is at least 108% and 125% margin (expressed as percent allowable growth) on the longeron and node dimensional change against the 56 µm allocation. **Based on this, the requirements for Milestone 7A are met.**

There are some features of the data in Figure 8 and Figure 9 that warrant further study:

- Longeron 1 exhibits a change in its critical dimension by 19 µm at the "Post-Ship" measurement, and then a recovery to about 10 µm in the subsequent measurements. This may be due to strain from moisture absorption. Carbon-fiber/cyanate-ester composites have a coefficient of moisture expansion (CME) of approximately $85 \times 10^{-6}$ per % of water absorbed by mass and a maximum water absorption capacity of approximately 0.30% [12], which would lead to a maximum strain of $25.5 \times 10^{-6}$, equivalent to a change in longeron critical dimension of 25 µm. Longeron 1 had been shipped to NGIS in San Diego, California and returned to Louisville, Colorado just prior to this measurement, and may have absorbed moisture while in San Diego. San Diego is historically more humid that Louisville.
- Node 2 exhibits a permanent shift in its critical dimension by about 15 µm following the thermal soak at 40 °C for 72 hours. Node 3, on the other hand, does not display this shift. Examining the measured dimensional changes on the 'A' and 'B' sides of node 2 (see Figure 20 in Appendix F), it can be seen that only side 'B' of node 2 exhibits these dimensional changes. Possible mechanisms include a local debond between the epoxy and the brass bushing on side 'B' (Milestone 8A analysis showed local stress concentrations due to thermal strain at the bushing-epoxy interface, and for this reason, the bushing material was updated to Invar; this updated design was only used for Milestone 8A thermal deformation testing), strain due to moisture absorption, or some other inelastic effect.

Variations in the dimensional change, from measurement to measurement, seem to exhibit similar trends across the two test articles for both the longeron and the node. A large portion of these variations are expected to be due to the thermal strain of the MicroVu machine, which would appear as a systematic effect for measurements of all test articles. This is because after a given number of thermal cycles, all test articles are measured over a relatively short period of time, and, given the thermal inertia of the granite bench, the MicroVu thermal strain is expected to be mostly the same for all measurements conducted over this period.

# 8 Conclusions

This report demonstrates that critical components of a perimeter truss bay have sufficient thermal cycle stability to meet KPP7. Both the longeron and the node were demonstrated to have thermal cycle stability better than 56 µm with 108% and 125% margin, respectively. This performance is consistent with thermal cycle stability of a truss bay better than 79.5 µm. This is then consistent with petal position accuracy error components being within the allocations presented in Table 1 – 62 µm radial bias, 260 µm radial random, 80 µm tangential random – that meet KPP7.

## 8.1 Future Work

To provide early assessment regarding thermal-cycle-stability of the longerons and nodes when loaded, both in the deployed and stowed configurations, test articles will undergo loaded testing. Coupon-level material testing of strain due to moisture expansion will also be conducted. These activities, and the work presented in this report, are pathfinders for the tests that will be done to meet Milestone 7B of the S5 activity, which is listed here for reference [1]:

> Truss Bay assembly demonstrates dimensional stability with thermal cycles (deployed) and storage consistent with a total pre-launch petal position accuracy within ± 300 µm.

Work addressing Milestone 7B will include experimental verification of the stability of a *truss bay assembly* through thermal cycling. Further investigation will inform the temperature range and the number of thermal cycles that will be used for testing for Milestone 7B. Additionally, we will consider using a more accurate metrology system (e.g. a MicroVu with temperature compensation) with low-CTE "truth rods" as reference control lengths.

## Acknowledgments

David Opland at Tendeg carried out the FEA of the IDS described in Appendix C.

This research was carried out at the Jet Propulsion Laboratory, California Institute of Technology, under a contract with the National Aeronautics and Space Administration.

## Acronyms

| | |
|---|---|
| CFRP | Carbon-Fiber-Reinforced Plastic |
| CME | Coefficient of Moisture Expansion |
| CNC | Computer Numerically Controlled |
| CSZ | Cincinnati Sub-Zero |
| CTE | Coefficient of Thermal Expansion |
| FEA | Finite Element Analysis |
| IDS | Inner Disk Subsystem |
| JPL | Jet Propulsion Laboratory |
| KPP | Key Performance Parameter |
| MS | Milestone |
| NGIS | Northrop Grumman Innovation Systems |
| OD | Outer Diameter |
| OS | Optical Shield |
| RSS | Root-sum-square |
| RTD | Resistance Temperature Detector |
| S5 | Starshade-to-TRL5 |
| SRM | Starshade Rendezvous Mission |
| TC | Thermal Cycle |
| TRL5 | Technology Readiness Level 5 |
| UD | Unidirectional |

## References

[1] Willems, P., "Starshade to TRL5 (S5) Technology Development Plan," Tech. rep., Jet Propulsion Laboratory, Dec. 2018.

[2] Arya, M., Webb, D., et al., "Starshade Technology Development Activity Milestone 7C: Demonstration of Deployment Accuracy of the Starshade Inner Disk Subsystem," Tech. rep., Jet Propulsion Laboratory, 2019.

[3] Webb, D., Bradford, S. C., et al., "Starshade Technology Development Activity Milestone 8A Verify Petal Position On-Orbit Stability," Tech. rep., Jet Propulsion Laboratory, 2019.

[4] Seager, S., Kasdin, N. J., et al., "Starshade Rendezvous Probe Study Report," Tech. rep., Feb. 2019.

[5] Gaudi, S., Seager, S., et al., "HabEx: Habitable Exoplanet Observatory Final Report," Tech. rep., Aug. 2019.

[6] Webb, D., Hirsch, B., Bach, V., Sauder, J., Bradford, S. C., and Thomson, M., "Starshade Mechanical Architecture & Technology Effort," *3rd AIAA Spacecraft Structures Conference*, San Diego, California, USA, Jan. 2016.

[7] Hirsch, B., Webb, D., and Thomson, M., "Starshade Deployable Inner Disk Structure Design and Development," *3rd AIAA Spacecraft Structures Conference*, San Diego, California, USA, Jan. 2016.

[8] Kasdin, N. J., Spergel, D. N., Vanderbei, R., Shaklan, S., Lisman, D., Thomson, M., Marks, G., Lo, A., and Macintosh, B., "Verifying Deployment Tolerances of an External Occulter for Starlight Suppression," Tech. rep., 2014.

[9] Arya, M., Webb, D., et al., "Demonstration of Deployment Accuracy of the Starshade Inner Disk Subsystem," *AIAA Scitech 2020 Forum*, Orlando, FL, Jan. 2020.

[10] Thomson, M., "The AstroMesh deployable reflector," *IEEE Antennas and Propagation Society International Symposium Digest*, Vol. 3, 1999, pp. 1516–1519.

[11] Micro-Vu Corporation, "EXCEL Measuring Center," 2007.

[12] European Cooperation for Space Standardization, "Structural materials handbook - Part 1: Overivew and material properties and applications," *Space engineering*, 2011.

[13] Pellegrino, S., "Analysis of prestressed mechanisms," *International Journal of Solids and Structures*, Vol. 26, No. 12, 1990, pp. 1329–1350.

[14] Pellegrino, S., "Structural computations with the singular value decomposition of the equilibrium matrix," *International Journal of Solids and Structures*, Vol. 30, 1993, pp. 3025–3035.

[15] Guest, S., "The stiffness of prestressed frameworks: A unifying approach," *International Journal of Solids and Structures*, Vol. 43, 2006, pp. 842–854.

[16] Renishaw, "RGH41 RGS40 linear encoder system," 2019.

[17] Webb, D., Steeves, J., et al., "Starshade Technology Development Activity Milestone 6A Verify Petal Shape on-Orbit Stability," Tech. rep., Jet Propulsion Laboratory, 2020.

[18] Hockman, A. and Kessler, D. W., "Thermal and Moisture Expansion Studies of Some Domestic Granites," *Journal of Research of the National Bureau of Standards*, Vol. 44, April 1950, pp. 395–410.

[19] Paquin, R. A., "Materials for Optical Systems," *Optomechanical Engineering Handbook*, edited by A. Ahmad, CRC Press LLC, 1999.

# A Original Allocation of KPP7 Instrument Contrast

| | **MS 7A, 7B** (µm) | **MS 7C, 7D** (µm) | **RSS total** (µm) | **Instrument Contrast** |
|---|---|---|---|---|
| Radial bias | 125 | 35 | 130 | $6.36 \times 10^{-13}$ |
| Radial random | 175 | 150 | 230 | $2.27 \times 10^{-13}$ |
| Tangential random | 75 | 120 | 142 | $1.35 \times 10^{-13}$ |
| Total | | | 300 | $1.00 \times 10^{-12}$ |

Table 5: Original sub-allocation of KPP7 contrast levels to components of the petal position accuracy error.

Table 5 shows the original sub-allocation of KPP7 instrument contrast that was presented in the Milestone 7C report [2]. For the present work, the petal position accuracy error allocations to Milestone 7A and 7B were updated from the values listed in Table 5 to those listed in Table 1: radial bias from 125 µm to 62 µm, radial random from 175 µm to 260 µm, and tangential random from 75 µm to 80 µm. These allocations were updated, once the relationship between bay length errors and petal position accuracy errors was understood, such that all petal position accuracy error components impose identical requirements on the bay length errors.

Note that the allocations to Milestone 7C and 7D were *not* changed.

# B Derivation of Requirements for Bay Length Errors

To compute the relationship between perimeter truss bay length errors and petal position errors, two approaches were used. An algebraic approach was used to relate bay length errors and the radial bias component of the petal position error, and a Monte Carlo approach was used to relate bay length errors to all components of petal position error. The algebraic approach resulted in a more conservative relationship between bay length errors and the radial bias component, and it was used to set requirements for the bay length errors. For the radial random and tangential random components of the petal position errors, the Monte Carlo approach was used to set requirements on bay length errors.

| | **Petal position error** (µm) | **Bay length error** (µm) | **Source** |
|---|---|---|---|
| Radial bias | 62 | 79.5 | Algebraic approach |
| Radial random | 260 | 79.5 | Monte Carlo analysis |
| Tangential random | 80 | 79.5 | Monte Carlo analysis |

Table 6: The chief components of the petal position errors as translated to equivalent perimeter truss bay length errors. All errors are written as $3\sigma$ values.

## B.1 Algebraic Approach for Relating Bay Length Errors and Radial Bias

Consider a 2D model of a perimeter truss as a $N$-sided polygon: the bays are the sides of the polygons. The error in the circumference (i.e. the difference between a perfect truss and an imperfect truss) is denoted as $\delta C$. It can be related to length errors $\delta L_i$ of the truss bays:

$$\delta C = \sum_{n=1}^{N} \delta L_i \tag{14}$$

For sufficiently large $N$, the error in the mean radius $\delta R$ of the vertices of the polygon (which is comparable to the petal position radial bias error) is related to the error in the circumference:

$$\delta R = \frac{\delta C}{2\pi} \tag{15}$$

$$\Rightarrow \delta R = \frac{1}{2\pi} \sum_{i=1}^{N} \delta L_i \tag{16}$$

Assuming that the bay length errors $\delta L_i$ are normally distributed with some standard deviation $\sigma(\delta L)$, the resulting standard deviation $\sigma(\delta R)$ of the radial bias error can be computed:

$$\sigma(\delta R)^2 = \left(\frac{1}{2\pi}\right)^2 N \sigma(\delta L)^2 \tag{17}$$

$$\Rightarrow \sigma(\delta R) = \frac{\sqrt{N}}{2\pi} \sigma(\delta L) \tag{18}$$

The $3\sigma$ requirement on the radial bias error is 62 µm, and, using the equation above with $N = 24$, this translates to a $3\sigma$ requirement on the bay length error of 79.5 µm.

## B.2 Monte Carlo Approach

Random bay length errors taken from a zero-mean distribution with some standard deviation $\sigma(\delta L)$ were injected into a pin-jointed perimeter truss structural model of the IDS (described in Appendix C) and the resulting variations in petal position errors were extracted. For a number of discrete values of the standard deviation of bay length error $\sigma(\delta L)$, ranging between 5 µm and 160 µm at the $3\sigma$ level, 500 random imperfect

trusses were generated, and the standard deviations in petal position error components over those 500 imperfect truss were computed.

The standard deviation in petal position error components computed thus is plotted with respect to the standard deviation in bay length errors in Figure 10, Figure 11, and Figure 12. These relations fit well to linear (in the case of the tangential random and radial bias components) and quadratic (in the case of the radial random component) models; these models are also plotted.

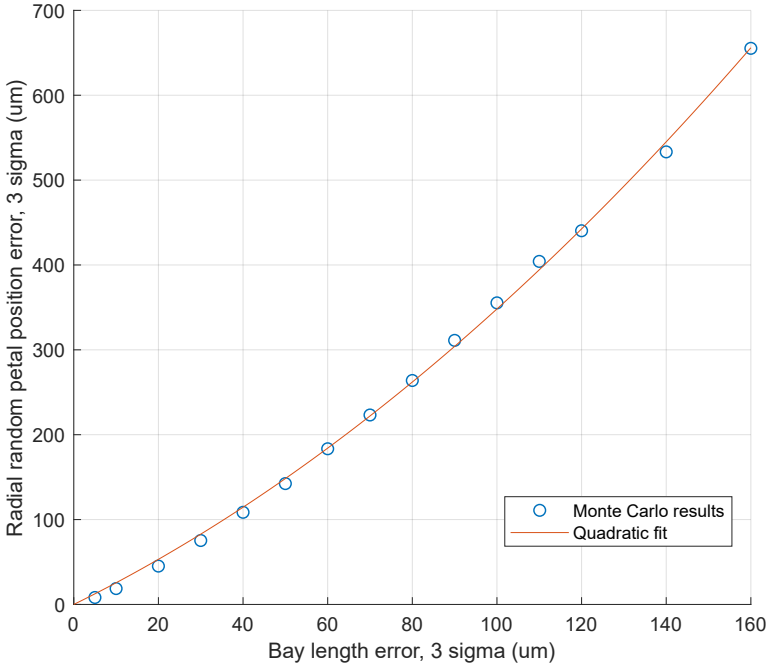


Figure 10: Bay length errors to radial random. Each circle represents results from 500 Monte Carlo runs.

The linear and quadratic fits are used to translate the $3\sigma$ petal position error requirements to $3\sigma$ bay length error requirements. To achieve radial random error below 260 µm, the bay length error must be below 79.5 µm. To achieve tangential random error below 80 µm, the bay length error must be below 79.5 µm. Finally, according to the model fits to the Monte Carlo results, to achieve radial bias error below 62 µm, the bay length error must be below 114.5 µm. However, the algebraic approach derived above (Equation (18)) imposes a tighter requirement of 79.5 µm on the bay length error to meet the same radial bias requirement, so that is used instead.

The reason the algebraic approach predicts higher radial bias than the Monte Carlo approach for the same bay length error is because the algebraic approach assumes a 2D model, whereas the Monte Carlo analysis uses a 3D model, where some of the net bias in perimeter truss circumference can be taken up by out-of-plane motion, thereby resulting in a smaller radial bias.

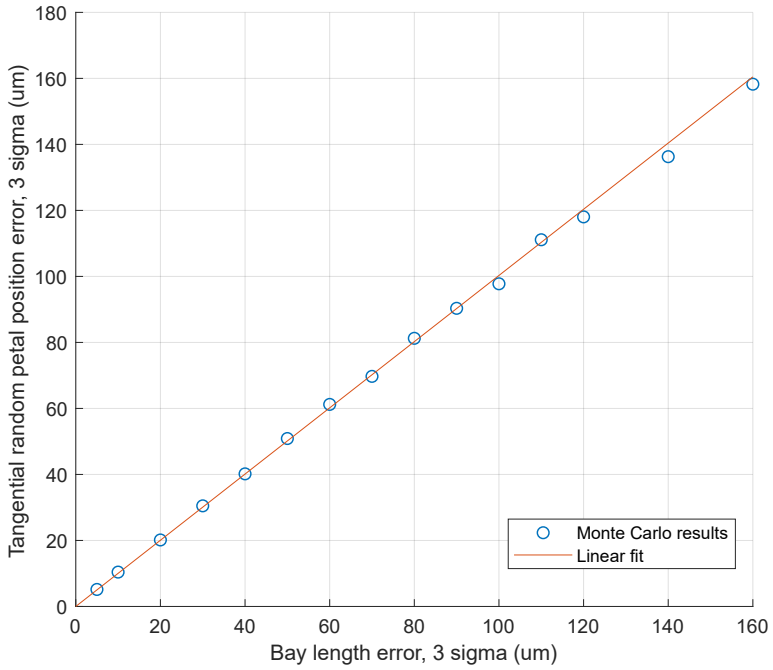


Figure 11: Bay length errors to tangential random. Each circle represents results from 500 Monte Carlo runs.

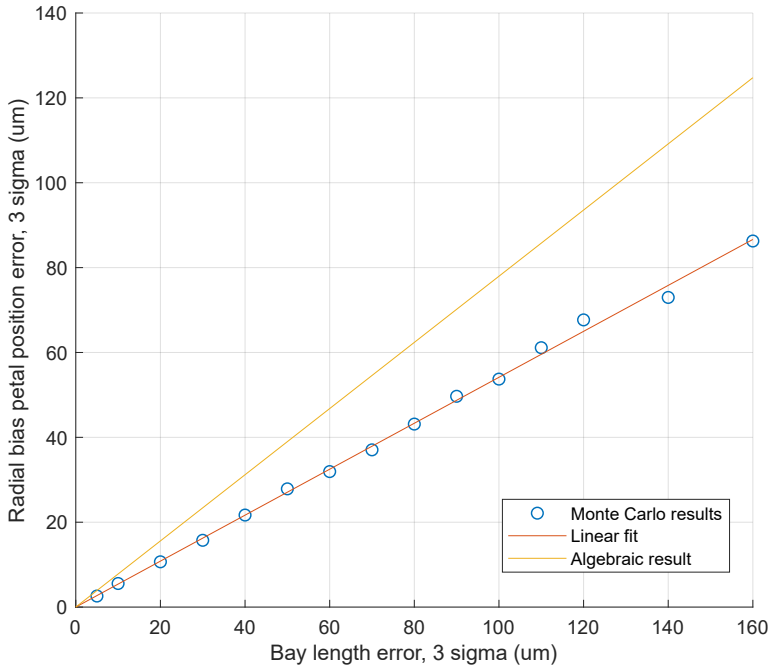


Figure 12: Bay length errors to radial bias. Each circle represents results from 500 Monte Carlo runs. The algebraic result is from Equation (18).

# C Structural Model of the Deployed IDS

As in [9, 2], the stiffness of the deployed IDS can be captured by a prestressed pin-jointed truss model [13, 14, 15]. The stiffness matrix $\mathbf{K}$ relates the nodal displacements $\mathbf{d}$ to the applied nodal forces $\mathbf{f}$:

$$\mathbf{Kd} = \mathbf{f} \tag{19}$$

$$\mathbf{K} = \mathbf{AGA}^T - \mathbf{A}\hat{\mathbf{T}}\mathbf{A}^T + \mathbf{S} \tag{20}$$

where $(\mathbf{AGA}^T)$ represents the material stiffness of the members, and $(-\mathbf{A}\hat{\mathbf{T}}\mathbf{A}^T + \mathbf{S})$ represents the stiffness due to prestress. $\mathbf{A}$ is the equilibrium matrix, $\mathbf{G}$ is a diagonal matrix of bar axial stiffnesses $EA/L$, $\hat{\mathbf{T}}$ is a diagonal matrix of bar tension densities $t/L$, and $\mathbf{S}$ is the stress matrix. The exact definitions and methods for constructing these matrices can be found in [15].

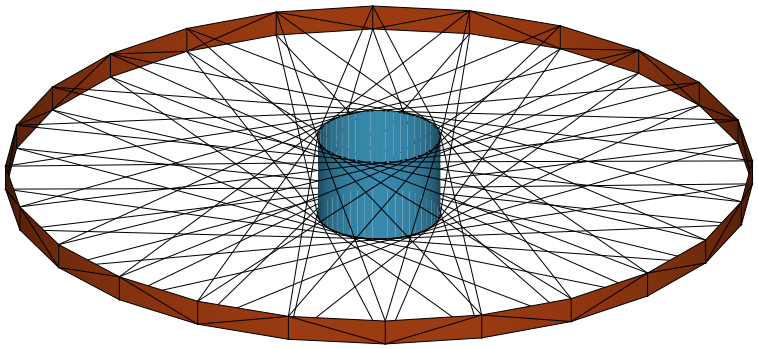

Figure 13: Structural model of the IDS.

The IDS prototype is not exactly a pin-jointed framework; however, the following simplifying assumptions makes the structure amenable to such analysis:

1. The truss node, which in reality is a stiff triangular structure, is represented by a single vertical bar.
2. The connections between the truss members – the longerons, the shorterons, the diagonals – and the truss nodes are assumed to be pin joints, incapable of transferring moments, whereas in reality these connections can transfer moments orthogonal to the axis of the revolute joint.

The structural model, illustrated in Figure 13, consists of 48 vertices at the truss, 2 for each of the 24 truss nodes, and 96 vertices at the hub, 4 for every truss bay. The truss nodes, the truss longerons and shorterons, the truss diagonals, and the spokes are represented as axially loaded bars. The vertices at the hub are held constrained in all 3 translational degrees of freedom, and forces are applied to the vertices at the truss. In the prestressed state, spoke tension is 71 N, longeron compression is 535 N, node tension is 11 N, and the diagonal is unstressed. Table 7 lists the axial stiffnesses of the members used for this analysis.

| | $E$ (GPa) | $A$ (mm$^2$) | $EA$ (N) |
|---|---|---|---|
| Longeron | 124 | 116 | $1.43 \times 10^7$ |
| Node | 69 | 293 | $2.03 \times 10^7$ |
| Diagonal | 124 | 59 | $7.30 \times 10^6$ |
| Spoke | | | $90.1 \times 10^3$ |

Table 7: Member axial stiffnesses used for the structural model.

This simplified structural model was validated using a much more detailed finite element analysis (FEA) model of the deployed flight-like IDS in Femap/Nastran. In the detailed FEA model, a $1 \times 10^{-6}$ strain (corresponding to a 1.24 µm growth) was applied to a single longeron in a single truss bay, and the resulting petal interface deflections were computed. This procedure determines the influence on petal interface locations for a unit error in the longeron length. The simplified pin-jointed truss model described above was then also

used to compute petal interface deflections due to a 1.24 µm growth of a single longeron in a single truss bay, and the resulting deflections of the nodal positions were computed. Figure 14 plots the radial and tangential components of these deflections for both the simplified truss model and the more detailed FEA model.

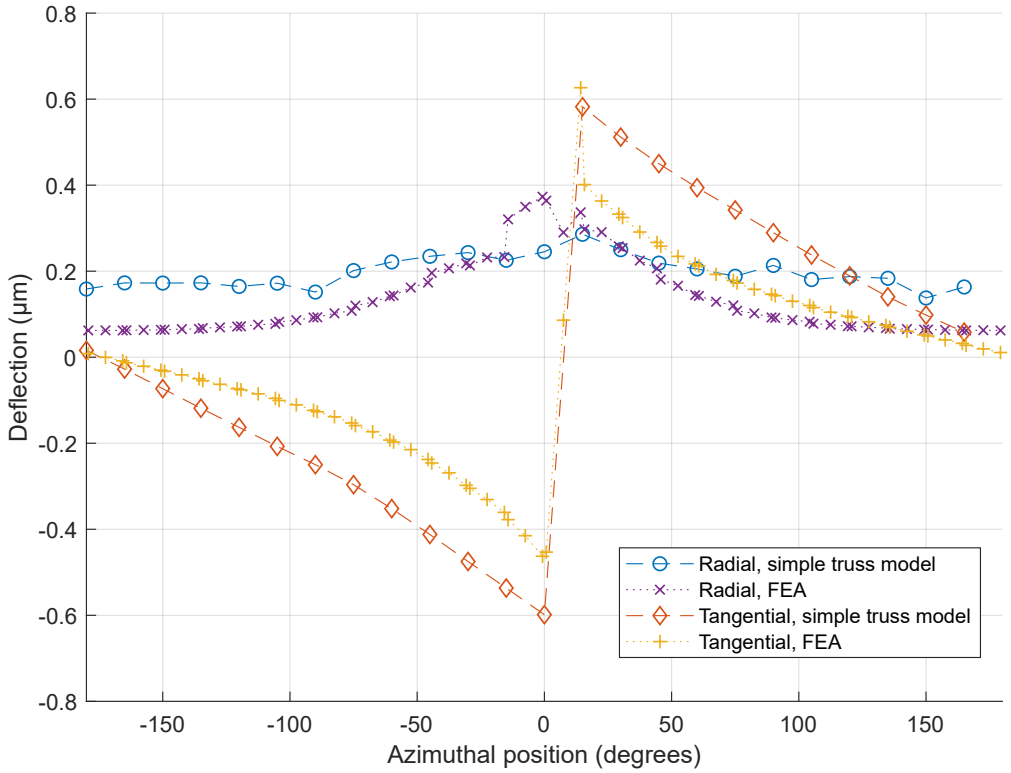


Figure 14: Comparison of petal interface deflections due to a $1 \times 10^{-6}$ strain in a single longeron in a single truss bay from the simplified truss model and a more detailed FEA model. The abscissa refers to the azimuthal position of the petal interface around the perimeter truss, with 0 being at the location of the strained longeron.

As can be seen, the simplified truss model predicts both the magnitude of the deflections and the character of the decay of the influence away from the position of the strained longeron.

Note that at the of level of deflections described in this report, both the FEA model and the simplified model are well within the limits of model linearity. As such, the effect of the strain in multiple truss bays is expected to be a linear superposition of the effects of strain in individual truss bays. It is for this reason it is sufficient to validate the simplified truss model using a single case of a unit expansion of a longeron.

# D Thermal Response of the MicroVu Measuring Machine

As described in Section 4.1, the MicroVu measuring machine uses as length references two linear encoders, one for each axis in the measurement plane. Each linear encoder is a Renishaw RGS40 scale [16], which is a ruled gold-plated steel tape that is bonded to a substrate; along the $x$-axis the substrate is a granite bench, and along the $y$-axis the substrate is a steel bar. Variations in substrate temperature cause substrate thermal strain, which translates to thermal strain of the linear encoders. This introduces length measurements errors. The errors along the $x$- and $y$-axes are orthogonal.

To compute these errors, consider the thermal strain of the linear encoder $\epsilon_{encoder} = \alpha\Delta T$ where $\alpha$ is the linear encoder CTE and $\Delta T$ is its temperature change. For a thermally invariant bar with reference length $L_{ref}$ (defined as the measured length when the encoder thermal strain $\epsilon_{encoder}$ is identically 0), the measured length $L_{measured}$ at some non-zero encoder thermal strain can be computed:

$$L_{measured} = \frac{L_{ref}}{1 + \epsilon_{encoder}} \tag{21}$$

Encoder thermal strains gives rise to an *apparent* measured strain $\epsilon_{apparent}$ of the thermally invariant bar:

$$\epsilon_{apparent} = \frac{L_{measured} - L_{ref}}{L_{ref}} \tag{22}$$

$$= \frac{-\epsilon_{encoder}}{1 + \epsilon_{encoder}} \tag{23}$$

To characterize this effect, a straightforward experiment was conducted: the temperature of the encoder substrates was varied and measured, and at each temperature, the length of a number of "truth bars" (with much lower CTE than granite or steel) was measured using the machine. From these measurements and Equation (22) and Equation (23), the apparent truth bar strain and the encoder strain at various temperatures can be calculated, thus yielding encoder CTEs.

Specifically, the "truth bars" were lengths of unidirectional pultruded CFRP (with a solid 7.94 mm-wide square cross-section) with measured CTE of $0.13 \times 10^{-6}\,^{\circ}\mathrm{C}^{-1}$ in a $17\,^{\circ}\mathrm{C} \pm 10\,^{\circ}\mathrm{C}$ temperature range (which encompasses the experimental conditions). Similar lengths of pultruded CFRP were used to make battens for the petal prototype for Milestones 5A and 6A. The CTE of these members was measured for Milestone 6A [17] at the Interferometric Metrology Facility at Northrop Grumman Innovation Systems.

For the present experiment, four truth bars were used, two for each axis; Figure 16 shows the location of the truth bars. The truth bars oriented along the $x$-axis are labeled X1 and X2, and were 1.98 m long, and the truth bars along the $y$-axis are labeled Y1 and Y2, and were 1.52 m long. The truth bars were elevated above the MicroVu bed, and supported in a quasi-kinematic fashion: pinned at one end, attached to a low-friction slider on the other, with two machined cylindrical rollers preventing sagging in the span while minimizing axial loads into the truth bar. The truth bars were not moved over the course of this experiment.

Optical targets were bonded to the truth bars to allow for precise length measurements. Figure 15 shows one of these targets. Each target has high-contrast features that allow for the precise measurement of the location of the center of the target using the MicroVu software. Seven equally spaced optical targets were bonded to the X1 and X2 truth bars, and six equally spaced optical targets were bonded to the Y1 and Y2 truth bars.

The temperature of the MicroVu was varied over a 4.5 °C range. Four resistance temperature detectors (RTDs) were attached to the granite table to measure its temperature changes, and two RTDs were attached to the steel bar to measure its temperature changes; Figure 16 shows the location of the RTDs. The temperature of the MicroVu was adjusted by changing the room thermostat setting; the room and the MicroVu were pre-cooled to about 16 °C over a weekend, the experiment began on a Monday, and the room temperature was slowly raised over the week. Table 8 shows the timeline of this experiment.

For each measurement listed in Table 8, the locations of the centers of optical targets on the truth bars were measured at the specified temperature. From this, the full length of each truth bar (i.e. the distance between the centers of the two end optical targets) can be computed. The baseline measurement was used as a reference to calculate apparent strain $\epsilon_{apparent}$ (using Equation (22)), which was then used to calculate encoder strain $\epsilon_{encoder}$ (using Equation (23)). The measured encoder strains are plotted against the measured changes in temperature in Figure 17. The temperature change is calculated as the mean of the changes in

Figure 15: Optical target attached to one of the truth bars.

| | Timestamp (MST) | Granite temperature (°C) | Steel temperature (°C) |
|---|---|---|---|
| Baseline | 2019.12.16 21:52 | 17.0 | 17.0 |
| Measurement 1 | 2019.12.17 10:39 | 17.6 | 18.4 |
| Measurement 2 | 2019.12.17 15:20 | 17.8 | 18.7 |
| Measurement 3 | 2019.12.18 10:07 | 18.8 | 19.6 |
| Measurement 4 | 2019.12.18 20:11 | 20.0 | 21.6 |
| Measurement 5* | 2019.12.19 10:19 | 20.5 | - |

Table 8: Timeline and temperatures for the MicroVu CTE measurement. *only X1 and X2 truth bars measured.

the relevant RTD temperatures; calculating relative change in RTD temperatures prior to taking the mean removes RTD temperature bias error.

In Figure 17, the temperature error bars capture the range of $\Delta T$ measured across the relevant RTDs, plus a random temperature error of 0.07 °C. The strain error bars are due to MicroVu length measurement uncertainty of ±5.5 µm; the relationship between encoder strain uncertainty $u(\epsilon)$ and length uncertainty $u(L)$ was calculated to be $u(\epsilon) = \sqrt{2}u(L)/L$, which gives strain uncertainty of $\pm 3.9 \times 10^{-6}$ for the longer truth bars along the $x$-axis, and $\pm 5.1 \times 10^{-6}$ for the shorter truth bars along the $y$-axis.

For each truth bar, only the longest lengths (i.e. the distance between the centers of the two end optical targets) were used for this analysis. This is because the strain uncertainty is the smallest for the longest lengths. The shorter lengths have higher strain uncertainty and were not used for the computation of CTEs; however, strains were computed using these shorter lengths and found to be consistent with the strains measured using the longest lengths.

Error in calculated encoder strain due to treating the truth bars as being invariant in length (i.e. with 0 CTE) when in reality they have some small CTE ($0.13 \times 10^{-6}\,°\mathrm{C}^{-1}$) is less than 3% for the $x$-axis, and less than 2% for the $y$-axis. Error in calculated encoder strain due to angular misalignment between the truth bars and the machine axes (which was measured to be less than 0.5°) is less than 0.003%.

As can be seen from Figure 17, the relationship between encoder thermal strain and delta temperature is linear. The slopes of the linear fits yield encoder CTEs: $4.9 \times 10^{-6}\,°\mathrm{C}^{-1}$ for the $x$-axis encoder affixed to the granite bench, and $11.2 \times 10^{-6}\,°\mathrm{C}^{-1}$ for the $y$-axis encoder affixed to the steel bar. (Standard errors on the coefficients of the linear fits are $0.1 \times 10^{-6}\,°\mathrm{C}^{-1}$ for the $x$-axis and $0.3 \times 10^{-6}\,°\mathrm{C}^{-1}$ for the $y$-axis.) These

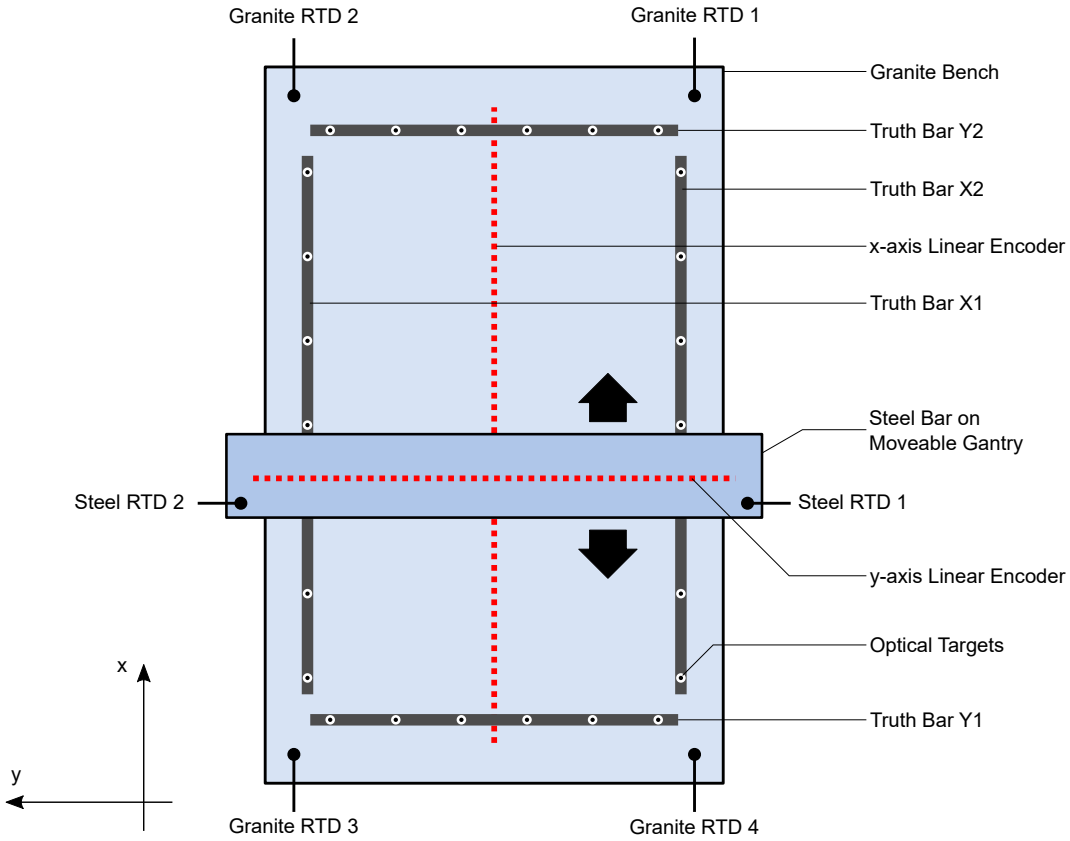


Figure 16: Schematic of the MicroVu instrumented for CTE measurement of the two linear encoders.

values compare well to accepted CTE values of the substrate materials to which the corresponding linear encoders are mounted: granite for the $x$-axis (reported CTE between $4.8 \times 10^{-6}\,^{\circ}\mathrm{C}^{-1}$ and $8.3 \times 10^{-6}\,^{\circ}\mathrm{C}^{-1}$ [18]) and steel for the $y$-axis (reported CTE between $8.5 \times 10^{-6}\,^{\circ}\mathrm{C}^{-1}$ and $14.7 \times 10^{-6}\,^{\circ}\mathrm{C}^{-1}$ [19]).

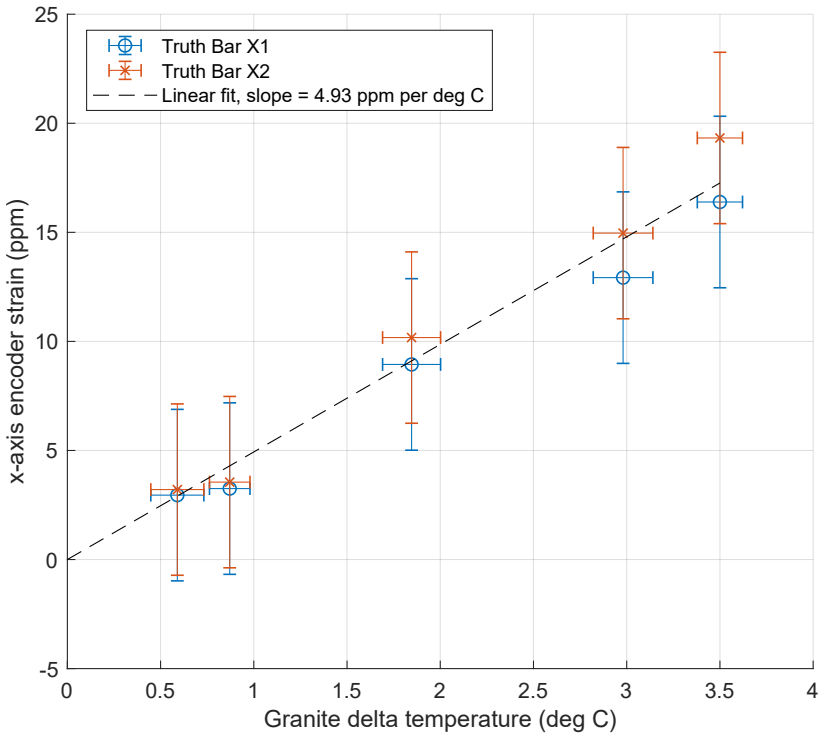


(a) $x$-axis encoder

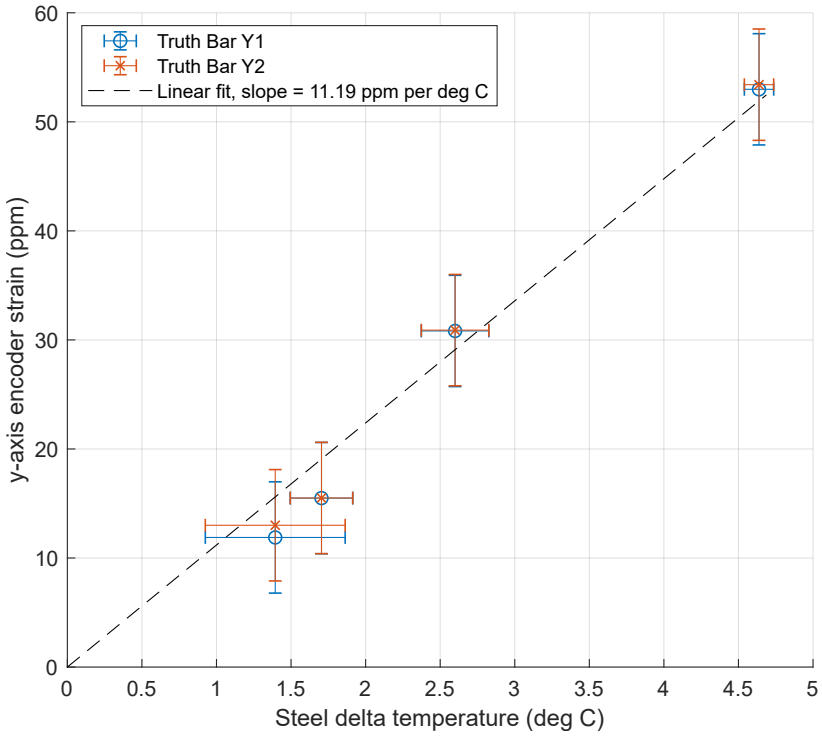


(b) $y$-axis encoder

Figure 17: Measured CTE of the MicroVu encoders.

# E Recorded Temperatures during Thermal Cycling

| **End Date** | **Number of cycles** | **Max. temp.** (°C) | **Min. temp.** (°C) |
|---|---|---|---|
| 2019.06.05 | 10 | 70.9 | -28.1 |
| 2019.06.13 | 10 | 70.4 | -26.8 |
| 2019.07.12 | 5 | 71.2 | -24.9 |
| 2019.12.07 | 10 | 69.2 | -24.4 |
| 2019.12.09 | 10 | 70.0 | -24.7 |
| 2019.12.11 | 10 | 70.3 | -24.8 |

Table 9: Sequence of longeron thermal cycles, and the maximum and minimum test article temperatures recorded during those thermal cycles.

| **End Date** | **Number of cycles** | **Max. temp.** (°C) | **Min. temp.** (°C) |
|---|---|---|---|
| 2019.04.22 | 10 | 67.9 | -19.8 |
| 2019.11.11 | 10 | 73.2 | -19.1 |
| 2019.12.05 | 10 | 70* | -25* |
| 2019.12.07 | 10 | 71.5 | -26.9 |
| 2019.12.09 | 10 | 71.3 | -27.0 |

Table 10: Sequence of node thermal cycles, and the maximum and minimum test article temperatures recorded during those thermal cycles. *estimated temperatures based on program settings. These temperatures were not recorded because of a hardware malfunction.

# F Dimensional Changes on Sides 'A' and 'B' of the Test Articles

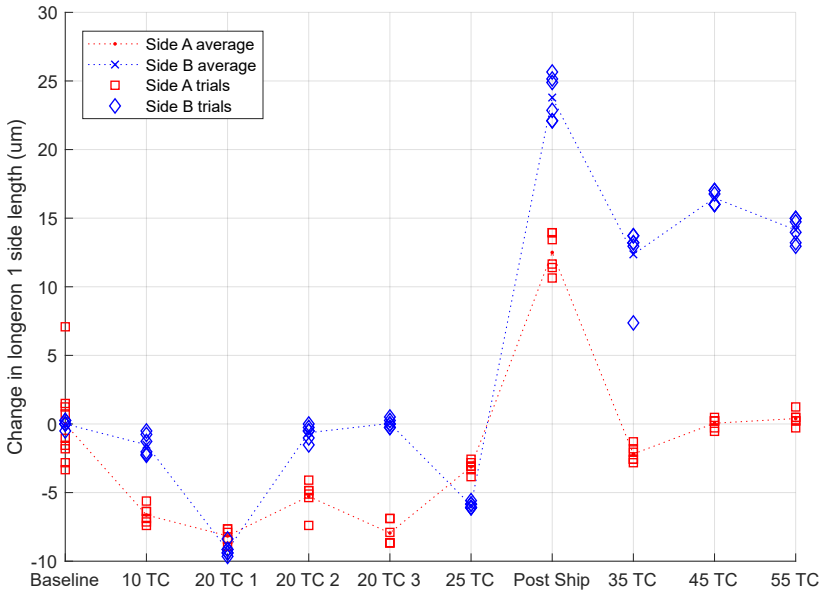


Figure 18: Change in critical dimensions on the 'A' and 'B' sides of longeron 1.

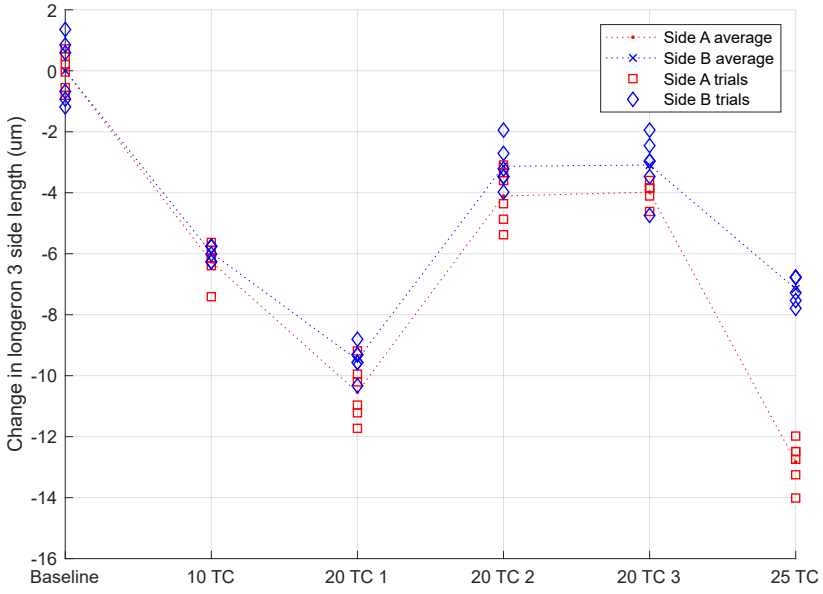


Figure 19: Change in critical dimensions on the 'A' and 'B' sides of longeron 2.

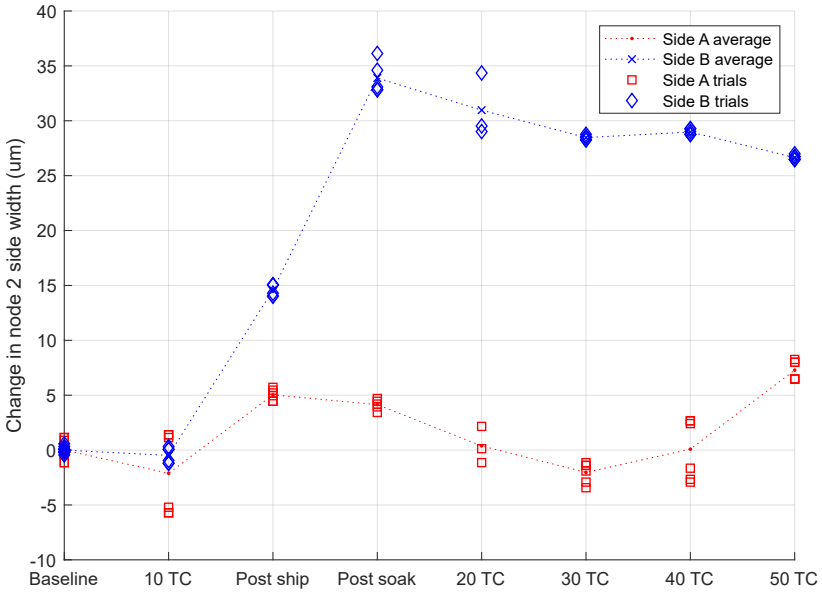


Figure 20: Change in critical dimensions on the 'A' and 'B' sides of node 2.

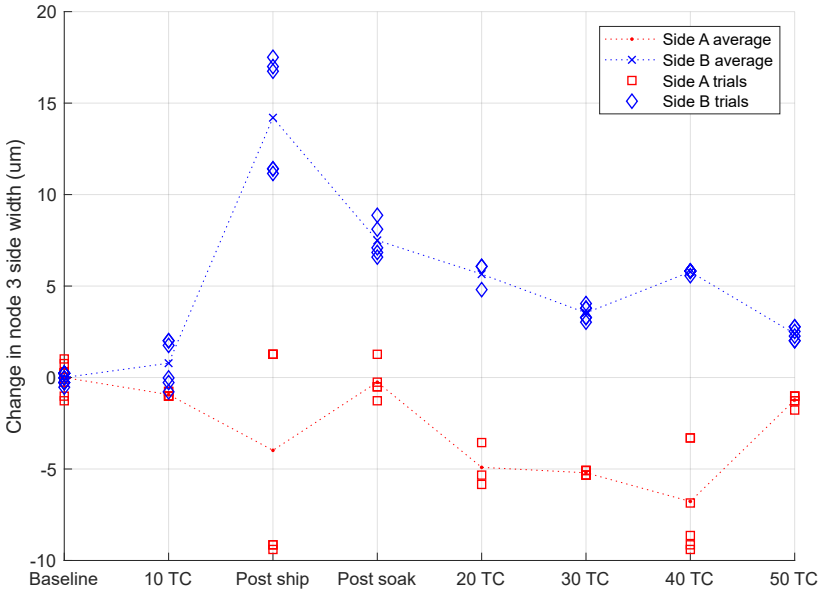


Figure 21: Change in critical dimensions on the 'A' and 'B' sides of node 3.

# G Expected Starshade Thermal Cycles

Table 11 summarizes the expected starshade mission temperature cycles, binned into 3 categories:

1. Less than 5 very large temperature cycles associated with launch and starshade deployment about one month later,
2. Less than 50 large temperature cycles associated with SRM retarget maneuvers and similar maneuvers for initial rendezvous or fault recovery, and
3. Less than 500,000 cycles associated with spinning, at different rates before and after deployment.

Following a stepwise experimental approach, the present Milestone 7A activity focuses on category 2. The follow-on Milestone 7B activity will thoroughly analyze all thermal cycle cases and establish a revised test plan accordingly. It is understood that a flight starshade will be subject to pre-launch qualification testing, which will encompass (with margin) the temperature extremes expected in flight; however TRL5 testing is not expected not include thermal testing to the levels of flight qualification programs.

| **Category** | **Scenario** | **Expected temp. range** | **Expected number of cycles** |
|---|---|---|---|
| Large | Launch<br>Starshade deployment | TBD | $\leq 5$ |
| Medium | Retarget maneuvers<br>Rendezvous<br>Fault recovery | $-25\,^{\circ}\mathrm{C}$ to $75\,^{\circ}\mathrm{C}$ | $\leq 50$ |
| Small | Pre-deploy 3 rpm spin<br>Post-deploy 0.33 rpm spin | $\leq 2\,^{\circ}\mathrm{C}$ | $\leq 500{,}000$ |

Table 11: Sequence of longeron thermal cycles, and the maximum and minimum test article temperatures recorded during those thermal cycles.

A number of assumptions are inherent in Table 11. The launch trajectory is direct to Earth-Sun-L2 in similar fashion to the James Webb Space Telescope (JWST). Prior to separation, the launch vehicle will spin up the starshade to about 3 rpm and point the starshade $\pm 90^{\circ}$ from the Sun, with the precise direction to be specified. Deployment may include spin-rates from 30 rpm down to 0 rpm, and also a period with attitude control disabled and possibly variable pointing, although experience with Astromesh antenna deployments suggests otherwise. Trajectory correction maneuvers and orbit insertion are all of relatively small $\Delta V$ and assumed to be executed in vector mode, without a thermal cycle.

Additional orbit maintenance maneuvers are periodically executed although the current concept is to integrate them into the retarget maneuver. If this is not the case, and orbit maintenance maneuvers are separate from retarget maneuvers they are also of relatively small $\Delta V$ and can be executed in vector mode with no additional thermal cycles. Science mode pointing can be $40^{\circ}$ to $83^{\circ}$ from the Sun, while retarget pointing can be $0^{\circ}$ to $83^{\circ}$ from the Sun. Fault mode cases also need to be considered with potential pointing between $0^{\circ}$ to $90^{\circ}$ from the Sun.

Additionally, category 2 currently corresponds to the Starshade Rendezvous Mission (SRM); for HabEx, there will likely be more than 100 retarget maneuvers.

# H Effect of Coordinated Deformation Modes of the Inner Disk

Errors in petal position degrade instrument contrast. The petal position error profile (the rigid body petal position errors as a function of angular location around the inner disk) is expressed as a sum of unit translations and rotations of individual petals.

We compute the instrument contrast sensitivity due to random normal distributions of petal position errors. The total contrast degradation is calculated based on the expected amplitude of these error distributions and the computed sensitivities.

Coordinated deformation modes of the inner disk structure (e.g., ellipticity, trefoil, etc.) also result in instrument contrast degradation. However, these modes can be expressed as a linear sum of individual petal translations and rotations. As such, in computing total instrument contrast allocations, we do not add contrast contributions from coordinated deformation modes to avoid "double counting" instrument contrast degradation.

This is a conservative approach, especially since contrast sensitivity to coordinated deformation modes is lower than contrast sensitivity to random distributions of unit petal motions. Table 12 shows the instrument contrast degradation due to 1 mm rms amplitudes of random petal location error distributions and coordinated modes. As can be seen, randomly distributed petal position errors create larger contrast degradation than coordinated modes.

| **Error term** | **Instrument contrast** |
|---|---|
| **Random distributions** | |
| Radial random | $6.0 \times 10^{-11}$ |
| Radial tangential | $9.1 \times 10^{-11}$ |
| **Coordinated modes** | |
| Elliptical | $5.0 \times 10^{-11}$ |
| Trefoil-like | $1.3 \times 10^{-11}$ |
| Quatrefoil-like | $1.1 \times 10^{-12}$ |
| Pentafoil-like | $3.0 \times 10^{-14}$ |
| Hexafoil-like | $3.0 \times 10^{-15}$ |
| Higher order | $< 5.5 \times 10^{-14}$ |

Table 12: Instrument contrast degradation for 1 mm rms amplitude for various petal error distributions.

To verify our approach, we will, in future studies, evaluate observed coordinated mode amplitudes and verify low contrast contributions due to these coordinated modes.